# Spatial and temporal variations in basal melting at Nivlisen ice shelf, East Antarctica, derived from phase-sensitive radars

**Katrin Lindbäck[1], Geir Moholdt[1], Keith W. Nicholls[2], Tore Hattermann[1], Bhanu Pratap[3], Meloth Thamban[3], Kenichi Matsuoka[1]**

[1] Norwegian Polar Institute, Framsentret, Postboks 6606, Langnes, 9296 Tromsø, Norway.

[2] British Antarctic Survey, Natural Environmental Research Council, High Cross, Madingley Rd, Cambridge CB3 0ET, UK.

[3] ESSO-National Centre for Polar and Ocean Research, Ministry of Earth Sciences, Headland Sada, Vasco-da-Gama, Goa 403 804 , India.

*Correspondence to:* Katrin Lindbäck (katrin.lindback@npolar.no)

**Abstract**

Thinning rates of ice shelves vary widely around Antarctica and basal melting is a major component in ice shelf mass loss. In this study, we present records of basal melting, at unique spatial and temporal resolution for East Antarctica, derived from autonomous phase-sensitive radars. These records show spatial and temporal variations of basal melting in 2017 and 2018 at Nivlisen ice shelf, central Dronning Maud Land. The annually averaged basal melt rates are in general moderate (~0.8 m $yr^{-1}$). Radar profiling of the ice shelf shows variable ice thickness from smooth beds to basal crevasses and channels. The highest basal melt rates (3.9 m $yr^{-1}$) were observed close to a grounded feature near the ice-shelf front. Daily time-varying measurements reveal a seasonal melt signal 4 km from the ice-shelf front, at an ice draft of 130 m, where the highest daily basal melt rates occurred in summer (up to 5.6 m $yr^{-1}$). In comparison with wind, air temperatures, and sea-ice cover from reanalysis and satellite data the seasonality in basal melt rates indicates that summer-warmed ocean surface water was pushed by wind beneath the ice-

shelf front. We observed a different melt regime 35 km into the ice-shelf cavity, at an ice draft of 280 m, with considerably lower basal melt rates (annual average of 0.4 m $yr^{-1}$) and no seasonality. We conclude that warm deep ocean water at present has limited effect on the basal melting of Nivlisen. On the other hand, a warming in surface waters, as a result of diminishing sea-ice cover has the potential to increase basal melting near the ice-shelf front. Continuous in situ monitoring of Antarctic ice shelves is needed to understand the complex mechanisms involved in ice shelf–ocean interactions.

## 1 Introduction

The Antarctic contribution to global sea-level rise has increased by a factor of five in the past two decades (The IMBIE Team, 2018). Over 80 % of the grounded ice in Antarctica drains out into floating ice shelves (Dupont and Alley, 2005). The thinning rates of these ice shelves vary widely around the continent (Paolo et al., 2015). The mass balance of an ice shelf is the sum of the ice gain and loss; ice gain comprises the advective input from ice across the grounding zone (where ice detaches from the bed and becomes afloat), snow accumulation, and marine ice accretion. Ice loss encompasses surface melting and sublimation, basal melting from the ocean underneath the floating ice shelf, and iceberg calving at the ice front (Bamber et al., 2018). A negative mass balance can affect ice-shelf stability, where a net mass loss reduces back stresses on grounded ice upstream, leading the tributaries to flow faster (Reese et al., 2018). Understanding controls on the mass balance of ice shelves around Antarctica is therefore the key to gain a better understanding of the continent's present and future contribution to global sea-level rise.

Iceberg calving occurs irregularly in time and can have dramatic effects on ice shelf mass balance when it occurs (Hogg and Gudmundsson, 2017). At present, iceberg calving comprises approximately half of the mass loss from the Antarctic Ice Sheet, where the other half comes from basal melting (Depoorter et al., 2013; Rignot et al., 2013). Basal melting is not uniform and depends on the ocean properties in the vicinity of the ice shelf, the topography of both the ocean bed and the ice-shelf base. Jacobs et al. (1992) described how different water masses can melt the ice shelf from below:

In mode 1, ocean water with temperatures at the surface freezing point provides heat for melting of deeper parts of the ice base, because the pressure-melting point of the ice is decreased to lower temperatures at depth. Basal melting at the deep grounding zones can be high and often occur at basal channels (e.g., 22 m $yr^{-1}$ for Ross Ice Shelf; Marsh et al., 2016); however, substantial marine-ice accretion reduces the net melting below these large ice shelves when the rising melt plume from the grounding zone super-cools and refreezes on the ice-shelf base at shallower depths (Joughin and Vaughan, 2004). Since these cold shelf waters provide a limited source of ocean heat (Darelius and Sallée, 2017), average basal melt rates are often low for the largest ice shelves (e.g., 0.3 m $yr^{-1}$ for Ronne Ice Shelf; Rignot et al., 2013).

In mode 2, ice shelves melt from the presence of warm circumpolar deep water intrusion (Jacobs et al., 1992). The rapid retreat and high thinning rates of glaciers in Antarctica have been attributed to the presence of warm circumpolar deep water below ice shelves in the Amundsen Sea sector of West Antarctica (Pritchard et al., 2012; Rignot et al., 2013). Circumpolar deep water surrounds the Antarctic continent, flowing clockwise with the Antarctic Circumpolar Current and is abundant near the continental shelf of West Antarctica. Circumpolar deep water accesses the deep bases of ice shelves directly through cross-continental submarine troughs, causing the higher basal melt rates; for example, Rignot et al. (2013) found Pine Island Ice Shelf to have an average melt rate of 16 m $yr^{-1}$. In East Antarctica, basal melting has been linked to circumpolar deep water intrusion only at Totten Ice Shelf, where annual basal melt rates reached ~11 m $yr^{-1}$ (Rignot et al., 2013; Rintoul et al., 2016). Farther west, in the Weddell Sea sector a cooler modified version of circumpolar deep water is advected along the coast (Dong et al., 2016; Ryan et al., 2016).

In mode 3, ice shelves can melt at shallow depths in the vicinity of their ice fronts when summer-warmed surface water is pushed by wind and tides under ice shelves (Jenkins and Doake, 1991; Makinson and Nicholls, 1999; Sverdrup, 1954; Zhou et al., 2014). Antarctic surface water has been observed under the Ross Ice Shelf in West Antarctica (Malyarenko et al., 2019; Stern et al., 2013; Stewart et al., 2019) and at Fimbulisen in East Antarctica (Hattermann et al., 2012), suggesting it may be a more important process in basal melting than previously thought. Spatial patterns and relative magnitudes of all these three modes of basal melting

remain largely unknown. Numerical modelling, however, indicates that the response of basal melting in the future strongly depends on the surface air warming (Kusahara and Hasumi, 2013). Future basal melting in Antarctica will therefore reflect the integrated response to changes in circumpolar deep water temperatures and coastal processes that control its access onto the continental shelf (Thompson et al., 2018). The detailed interplay of these processes today and in a future climate are still a major source of uncertainty when evaluating the response of the Antarctic Ice Sheet to climate change (Adusumilli et al., 2018).

In this study, we measured basal melting at Nivlisen (70° S, 12° E) in central Dronning Maud Land, East Antarctica, using autonomous phase-sensitive radio-echo sounders (ApRES; Fig. 1). Phase-sensitive radars use a technique where the phase of individual internal ice reflectors is tracked, yielding time series of ice thickness change at high accuracy (~1 mm) and short time intervals (Corr et al., 2002; Nicholls et al., 2015). This technique has been used to measure basal and englacial properties of ice at several locations around Antarctica (e.g., Davis et al., 2018; Jenkins et al., 2006; Marsh et al., 2016; Stewart et al., 2019) and in Greenland (Vaňková et al., 2018). Our objective is to study the spatial and temporal variations of basal melting and to interpret the results using: (1) radar profiles of ice thickness, (2) in situ measured and satellite-derived or modelled ice flow speed and surface mass balance, and (3) atmospheric forcing from reanalysis data, sea-ice distribution, and ocean tides. The data imply that different modes of basal melting are present at Nivlisen. Our in situ measured data of basal melting complement satellite-derived maps of spatially-smoothed time-averaged basal melt rates, and will be a valuable data source for validation of ice shelf and ocean models.

## 2 Study area

Dronning Maud Land covers a large area of East Antarctica, and its 2000 km-long coast is characterized by extensive ice shelves interspersed with numerous ice rises and rumples (Fig. 1a). Ice rises are locations where ice-shelf flow is diverted around the grounded ice and are miniature ice caps with their own flow fields from the summit (Matsuoka et al., 2015). Ice rumples are smaller features that impose a disturbance on the ice-shelf flow, causing the ice to thicken upstream with extensive crevassing. Individual ice shelves are relatively small, but

extend close to, or even beyond, the continental-shelf break (Heywood et al., 1998). Basal melt rates from satellite data in Dronning Maud Land vary from near zero to 7 m $yr^{-1}$ (2003 to 2008; Rignot et al., 2013). The interior of this region is partly separated by high mountains, causing steep ice surface slopes from the continental plateau towards the coastal areas (Howat et al., 2019). The drainage basin of Nivlisen (27 700 $km^2$), including the grounded ice that drains to the ice shelf, has an estimated potential of raising global sea level by 8 cm (Rignot et al., 2019).

Nivlisen has an areal extent of ~7300 $km^2$ and forms a closed embayment between two larger promontory-type ice rises, Djupranen and Leningradkollen (Fig. 1b). Such grounded features are known to play vital roles in ice-shelf and ice-sheet dynamics over various timescales. For example, un-grounding of an ice rumple within the ice shelves of Pine Island and Thwaites Glacier is thought to be a major cause of the ongoing rapid retreat and thinning (Favier et al., 2012; Gladstone et al., 2012; Jenkins et al., 2010). Bawden Ice Rise near the edge of the Larsen C Ice Shelf helps maintain its stability, despite the collapse of neighbouring Larsen A and B ice shelves (Borstad et al., 2013; Holland et al., 2015). Nivlisen is also grounded at a series of smaller ice rises and rumples near the present ice front, as well as at a few ice rumples in the middle of the ice shelf (Moholdt and Matsuoka, 2015). The bathymetry under the ice shelf is unknown.

The average ice-shelf flow speed is 80 m $yr^{-1}$ (Rignot et al., 2011). Potsdam Glacier drains into Nivlisen from the southeast, with an average ice thickness of ~1000 m (Fretwell et al., 2013) and ice flow speed of ~50 m $yr^{-1}$ (Anschütz et al., 2007; Rignot et al., 2011). The satellite-derived estimate of the grounding-line flux for Nivlisen was 3.9 ± 0.8 Gt $yr^{-1}$ (2007–2008; Rignot et al., 2013). Elevated topography of the ice rises causes highly-variable local climate and surface mass balance gradients (Lenaerts et al., 2014). In addition, Nivlisen has large surface mass balance transitions from being positive in the firn area near the ice front to being negative in the blue-ice area near the grounding zone, with increased wind erosion, evaporation, and sublimation owing to katabatic winds (Horwath et al., 2006). Near the grounding zone, summer surface melting is sufficient to form supraglacial lakes and streams that may occasionally drain through the ice shelf (Kingslake et al., 2015), making Nivlisen potentially sensitive to hydrofracturing (Lenaerts et al., 2017). Rignot et al. (2013) estimated the

surface mass balance to be 1.8 ± 0.3 Gt $yr^{-1}$ (average 1979–2010) and the average calving flux to be 1.3 ± 0.4 Gt $yr^{-1}$ (2007–2008). These numbers together with the grounding-line flux mentioned earlier and a slightly positive net mass balance of 0.6 Gt $yr^{-1}$ (2003–2008) results in a residual net basal melt of 3.9 Gt $yr^{-1}$, or an average basal melt rate of 0.5 ± 0.2 m $yr^{-1}$ (Rignot et al., 2013). Thus, basal melting comprises ~75 % of the total outgoing flux, with the residual ~25 % attributed to iceberg calving.

The continental shelf extends ~100 km north of Nivlisen into the Lazarev Sea, and is roughly 500 m deep (Arndt et al., 2013; Fig. 1a). Carbon dating of laminated sediments on several locations near the ice shelf suggests that the ice front retreated to its present position by ~11 kyr ago (Gingele et al., 1997). North of Nivlisen lies Astrid Ridge (Fig. 1a), an undersea bathymetric feature extending from the Antarctic margin northward to ~65° S. Farther east lies Gunnerus Ridge (Fig. 1a), where circumpolar deep water is entrained into the Antarctic slope current. The circumpolar deep water is then cooled and modified to become warm deep water (Dong et al., 2016; Ryan et al., 2016) and flows westward along the continental slope to finally become entrained into the Weddell Gyre. The ice-shelf cavities in this region are separated from warm deep water by the Antarctic slope front, which is a pronounced transition zone over the narrow continental shelf between eastern shelf water and warm deep water. The slope front is mainly attributed to coastal downwelling caused by the prevailing easterly winds (Sverdrup, 1954; Thompson et al., 2018). The coastal dynamics that set the warm deep water depth along the continental-shelf break involves the balance between wind-driven Ekman overturning and counteracting eddy fluxes (Nøst et al., 2011; Thompson et al., 2014). These processes respond to changes in wind and buoyancy fluxes (Hattermann et al., 2014; Stewart and Thompson, 2016), including self-amplifying feedbacks of increased fresh water input from increased basal melting (Hattermann, 2018).

The Southern Ocean, including the Weddell Sea, has warmed over recent decades (Gille, 2002; Schmidtko et al., 2014) with the changes driven primarily by anthropogenic climate warming (Swart et al., 2018). Sea-ice cover has increased slightly since 1979 around Antarctica in general (De Santis et al., 2017), however extreme changes have occurred in recent years with record maxima three years in a row (2012 to 2014), followed by record minima 2016 and 2017

(Shepherd et al., 2018; Stuecker et al., 2017; Turner et al., 2015). Sea-ice fluctuations are strongly correlated with the dominant trends in Southern Hemisphere climate variability (Kwok et al., 2016; Kwok and Comiso, 2002), although further studies are needed to understand the drivers behind these fluctuations (Turner 2017). An increase in the seasonality of the easterly winds has been observed (Hazel and Stewart, 2019) and this may affect the formation and export of sea ice and the transport of surface waters and warm deep water to the continental shelf. All these pan-Antarctic observations may affect ocean water flow and consequent ice-shelf thinning in Dronning Maud Land and remains largely unknown.

## 3 Data and Methods

We conducted three field campaigns on Nivlisen and adjacent ice rises during the Antarctic austral summers, from mid-November until end of December, 2016 to 2018, with logistic support from the Indian Maitri and Norwegian Troll Station (Fig. 1a). In December 2016, we installed stakes for measurement of ice velocity and surface mass balance at 29 locations on Nivlisen and measured the ice thickness with an ApRES system (200–400 MHz), developed by the British Antarctic Survey (British Antarctic Survey, 2018; Nicholls et al., 2015; Fig. 1b): (1) 13 stakes were placed across the ice flow at a spacing of 10 km (profile A), (2) 10 stakes were placed along the ice flow towards a grounded ice rumple near the ice front with a spacing of 1 to 4 km (profile B), and (3) four stakes were placed along the ice flow towards the ice front at a spacing of 10 km (profile C). We also measured the ice-shelf thickness and basal structure with a low-frequency (5 MHz) radio-echo sounder along these three profiles. After the initial measurements, we installed similar ApRES systems at two locations for hourly measurements of basal melting and strain rates over the winter, each powered by a 12 V 114 Ah battery (Fig. 1b): (1) Four km from the ice-shelf front, called the “seaward site” hereafter, and (2) 35 km from the ice-shelf front, called the “landward site”. In December 2017 and 2018, we revisited and re-measured all ApRES sites to get averaged annual values of basal melting and strain rates and retrieved the time-series data from the two overwintering stations. Extensive crevassing prevented the three sites closest to the ice rumple (profile B, Fig. 1b) from being revisited in 2018.

### 3.1 Autonomous phase-sensitive radio echo sounder

ApRES uses the frequency-modulated continuous wave (FMCW) technique (Rahman, 2016). The instrument transmits a signal sweeping from 200–400 MHz over a period of 1 s to form a chirp (Nicholls et al., 2015). The system has a low-power consumption, with a power to the transmitter antenna of 100 mW. The averaged signal was amplified and de-ramped, a process where the received signal is mixed with a replica of the transmitted signal to extract differences in frequencies. The de-ramped signal was then filtered to amplify the higher frequencies preferentially, which enhanced weaker signals from more distant reflectors. Each sample consisted of 100 chirps, collected over a period of a few minutes. The data were digitized and stored on secure digital cards for further processing.

We processed the data following Brennan et al. (2014) and Nicholls et al. (2015). The data were Fourier transformed to give a complex signal amplitude as a function of delay time (or depth) assuming a constant propagation velocity of 168 m $\mu s^{-1}$. An amplitude cross correlation between the two returns, for a depth range within the firn layer (typically from 40 to 70 m), provided a vertical shift that approximately accounted for snow accumulation between the visits. The displacement of the reflectors between the two visits were then plotted as a function of depth (Supplements Fig. S1a). To give the necessary depth resolution, the phase of the signals was used to calculate the displacements by cross-correlating 4 m segments of the first profile with the complex conjugate of the corresponding segment of the second. Under the assumption of a constant vertical strain rate between the bottom of the firn layer and just above the ice base, we fit a straight line to the layer displacements. The correction for snow accumulation between the two visits included the coarse correction mentioned above and the precise correction inherent in the phase processing. This effect, together with the effect of the non-linear (with depth) displacements due to firn compaction, were contained within the intercept at the vertical axis. Thus the basal melt was given by the deviation of the displacement of the basal reflection from the straight line fit (Supplements Fig. S1b). The error in the calculated strain was estimated using the quality of fit of the linear regression. The uncertainty in the melt rate was obtained by combining the uncertainty in the strain rate with the uncertainty in the change in the range to the basal reflector, deduced from the signal-to-noise ratios of the two basal reflections.

To calculate the hourly melt rate time series for the two overwintering sites (Fig. 1b), we tracked the basal reflector using phase-coherent processing. This allowed us to determine the speed of motion of the ice base with respect to the antenna, which we hereafter call the thinning rate. To remove the component of ice-column vertical strain rate caused by tidal variations, we filtered the basal vertical speeds with a 36 h low-pass filter. We then removed an annual average vertical strain rate from the filtered basal motion, resulting in net basal melt rates. We assumed that, at periods longer than 36 hours, the variability in strain rate is small compared with the variability in basal melt rate.

### 3.2 Low-frequency radar profiling

We collected ~180 km of continuous radio-echo sounding profiles on Nivlisen to measure ice thickness and englacial and basal structure (profiles A, B, and C; Fig. 1b). We used a common-offset impulse radar system (Dowdeswell and Evans, 2004) based on the radar developed by Matsuoka et al. (2012) and processing steps following Lindbäck et al. (2014). We used half-wavelength dipole antennas with a 5 MHz centre frequency, using a Kentech impulse transmitter with an average output power of 35 W. The transmitter and receiver systems were mounted on two sleds and towed behind a snowmobile at a speed of ~10 km $h^{-1}$. We positioned the measurements using data from a code-phase global positioning system (GPS) receiver mounted on the radar receiver box 20 m in front of the common mid-point of the antennas along the travelled trajectory of the snowmobile. We post-corrected the height using the Canadian precise point-processing service (CSRS-PPP; Natural Resources Canada, 2017) from a kinematic carrier-phase dual-frequency GPS receiver mounted on the snowmobile. The radar measurements had an average trace spacing of ~5 m.

Several corrections and filters were applied to the radar data: (1) dewow and bandpass filters, to remove unwanted frequency components in the data, (2) depth-variable gain function, and (3) normal move-out correction to correct for antenna separation, including adjusted travel times for the trigger delay. The basal returns were digitized semi-automatically with a cross-correlation picker at the first break of the bed reflection (Irving et al., 2007). We calculated ice thickness from the picked travel times of the bed return using a constant radio-wave velocity of 168 m $\mu s^{-1}$ for ice. We added a correction term of 2 m to account for the faster propagation in

the firn. The firn had a depth of ~50 m, derived from the ApRES internal reflectors (Supplements Fig. S1c). To show the depth of the base of the ice shelf in the water column we calculated the ice draft from the ice thickness by subtracting the surface elevation, using an EIGEN-6C4 mean geoid height of 17 m above the ellipsoid (Förste et al., 2014). We estimated the error in ice thickness by standard analytical error propagation methods (Lapazaran et al., 2016; Taylor, 1996), outlined in Lindbäck et al. (2018). The estimation included the error in the radar acquisition and horizontal positioning error, where the radar acquisition errors comprised errors in radio-wave velocity and two-way travel time. Velocity can vary spatially, depending mainly on density. Errors in two-way travel time were estimated to be the range resolution, which is the accuracy of the measurement of the distance between the antenna and the bed. The average radar system error was estimated to 13.3 ± 1.2 m. The surface and base of the ice shelf is relatively flat, giving very small vertical errors from horizontal positioning (0.1 ± 0.2 m). The total error in ice thickness is presented together with the data in Sect. 4.

### 3.3 Ice flow and surface mass balance from stakes

Stake height over the surface was measured manually, and stake position was measured for 15 minutes using carrier-phase dual-frequency GPS receivers at 1 s logging interval. The stakes were revisited and measured in December 2017 and 2018. We processed the positions statically using CSRS-PPP (Natural Resources Canada, 2017). Snow density was measured at five locations on Nivlisen with an auger drill to a depth of 3 m and varied from 430–450 kg $m^{-3}$. We used the average snow density of 440 kg $m^{-3}$ and an ice density of 917 kg $m^{-3}$ to calculate the surface mass balance in ice equivalent. Ice flow velocity and surface mass balance were compared with estimates from satellite data (Rignot et al., 2011) and regional atmospheric modelling (van de Berg et al., 2006).

## 4 Results

In 2017, averaged annual basal melt rates, at 29 ApRES sites on Nivlisen (Fig. 1b), ranged from 0.12 ± 0.06 to 3.94 ± 0.04 m $yr^{-1}$ (Fig. 2a and Fig. 3), with a median value of 0.80 m $yr^{-1}$. The highest averaged annual basal melt rates were observed just upstream of an ice

rumple at the ice front. The lowest melt rates were observed in the central and eastern parts of the ice shelf. In 2018, averaged annual basal melt rates at 26 sites, ranged from 0.13 ± 0.06 to 1.48 ± 0.01 m $yr^{-1}$ (Supplements Fig. S2). In 2018, the median melt rate was 0.72 m $yr^{-1}$. Basal melt rates were slightly lower in the second year at 18 sites and for 8 sites slightly higher. The measurements in 2018 excluded three sites closest to the ice rumple, which had the highest melt rates in 2017, since we were not able to revisit these sites because of many crevasses in the area. Errors in basal melt rates were on average 0.023 m $yr^{-1}$ in 2017 and 0.025 m $yr^{-1}$ in 2018.

Strain rates had a median annual value of $-4.7 \times 10^{-4}$ $yr^{-1}$ in 2017 and $-4.6 \times 10^{-4}$ $yr^{-1}$ in 2018. The vertical strain-rate contribution to the average rate of thickness change was on average 22 %. The errors in strain were low, on average $6.2 \times 10^{-5}$ $yr^{-1}$ in 2017 and $7.1 \times 10^{-5}$ $yr^{-1}$ in 2018. For most parts of the ice shelf the strain rates were negative, meaning that the ice was thinning by longitudinal stretching, however, close to the ice rumple mentioned earlier (profile B; Fig. 3) we observed a transition from negative to positive strain rates (from $-5.4 \times 10^{-4}$ to $2.2 \times 10^{-2}$ $yr^{-1}$), with increasing compressional thickening of the ice towards the ice rumple. Positive strain rates were also observed for five sites 5–10 km upstream of the larger ice rises in the central and in the eastern part of the ice shelf (profile A; Fig. 3), indicating a far-reaching buttressing effect (distance up to ~30 ice thicknesses from the ice rises).

The two overwintering ApRES systems were used to derive time series of basal melt rates. The seaward overwintering site was located 4 km from the ice front and had an ice draft of 130 m, as measured with low-frequency radar. It operated for 14 months (from 11 Dec 2016–4 Feb 2018) before the battery failed. Thirty-six hour low-pass filtered basal melt rates at this site varied from ~0 to 5.6 m $yr^{-1}$, where the highest melt rates occurred in summer (29 Jan 2017; Fig. 4a). The landward overwintering site was located 35 km from the ice front and had an ice draft of 280 m. The data cover 22 months (from 4 Jan 2017–27 Nov 2018), excluding December 2017 when the instrument was used for measuring annual basal melt rates at other sites. At this site, 36 h low-pass filtered basal melt rates varied from ~0 to 2.0 m $yr^{-1}$, where the highest melt rates occurred in winter (12 Jun 2018; Fig. 5a).

Ice thickness, measured with low-frequency radar along profiles A, B, and C (Fig. 1b), varied from 160 to 330 m (Fig. 2b), with a median value of 260 m. We observed the thinnest ice

close to the ice front along profile C (Fig. 3) and the thickest ice in the southern-most part of the ice shelf along the same profile. The total error in ice thickness along the profiles, including radar system and positioning errors, varied between 10.6 and 15.7 m. The broad thickness pattern agrees with the gridded ice thickness of Bedmap2 (Fretwell et al., 2013), except close to the ice front in the western part (profile C), where the thickness of Bedmap2 is clearly too high (Fig. 2b), possibly due to errors in the input data or the interpolation between them. Ice draft varied from 120 to 280 m with a median value of 220 m (Fig. 3). We observed no significant relation between basal melting and ice draft. Several locations with undulating englacial layers, basal channels and crevasses were visible in the radar profiles (Fig. 3). Stake-measured ice flow speeds varied from 13 to 113 m $yr^{-1}$ in 2017, with an average value of 80 m $yr^{-1}$, agreeing with satellite estimates (Rignot et al., 2011; Fig. 2c). Surface mass balance values varied between 0.12 and 0.62 m i.e. $yr^{-1}$ in 2017 with an average of 0.45 i.e. $yr^{-1}$, higher than the modelled average estimates of 0.2 m i.e. $yr^{-1}$ (van de Berg et al., 2006), but with the same spatial pattern (Fig. 2d).

## 5 Discussion

In the following sections, we discuss the spatial and temporal variations in basal melting and compare our results with other studies from Antarctica. For each section, we also discuss strengths, limitations, and recommendations for future studies.

### 5.1 Spatial variations in melting

On Nivlisen, we observed the highest averaged annual basal melt rates (3.9 m $yr^{-1}$) close to a small (4.2 $km^2$) ice rumple at the ice front (Fig. 2a and Fig. 3). Similar basal melt rates (~4 m $yr^{-1}$) were inferred from satellite data nearby Bawden Ice Rise in the Antarctic Peninsula (Adusumilli et al., 2018). In modelling experiments, locally enhanced basal melt rates were caused by strong tidal currents in shallow regions (thin water column thickness) around the ice rise that increased the ice-ocean heat exchange (Mueller et al., 2012). At Nivlisen, we have no observations of ocean currents near the ice rumple, but the bathymetry must be shallow since the ice shelf grounds in this region. Ice-shelf thinning could potentially increase the water column thickness, leading to a negative (stabilizing) feedback on the melting by reducing the ocean

currents (Mueller et al., 2012, 2018; Padman et al., 2018). In terms of ice thickness change, the observed thinning from the basal melt is compensated by a positive vertical strain that implies compressional thickening towards the ice rumple (up to 4 m $yr^{-1}$). Thicker ice towards the ice rumple indicates a buttressing effect on the ice shelf (profile B; Fig. 3). We observed many crevasses in this region that made it, for safety reasons, difficult to revisit the three closest sites during the third field season (Dec 2018). Many ice shelves like Nivlisen are stabilized by pinning points at their ice fronts, which may be sensitive areas for future change. The effects of a future increased basal melting at the Nivlisen ice rumple are uncertain, and modelling work may indicate whether un-grounding of the ice would potentially lead to substantial loss of buttressing (Borstad et al., 2013).

Estimates of basal melt rates for Dronning Maud Land ice shelves have mainly used satellite techniques, modelling, or limited spatial or temporal coverage of in situ radar observations (Berger et al., 2017; Langley et al., 2014b). Fimbulisen is situated 400 km west of Nivlisen (Fig. 1a) at the outlet of Jutulstraumen, one of the largest ice streams in Dronning Maud Land. Below the deep keel from Jutulstraumen (300–400 m ice draft), time-averaged basal melt rates of several meters per year were observed, whereas at the shallower parts of the ice shelf (200–300 m ice draft), lower melt rates were observed (Langley et al., 2014a). In addition, annual-average basal melt rates were modelled to be near zero for large areas (Hattermann et al., 2014). Hattermann et al. (2014) hypothesized that basal melting (melt mode 1, Sect. 1) occurred at the deepest parts of Fimbulisen (below ice drafts of 400 m). The rising melt plume caused marine accretion at shallower depths closer to the ice front, which together with seasonal melting from summer-heated surface water (melt mode 3, Sect. 1), resulted in the low net basal melt rates. The seasonal marine-ice formation was inferred from an ice-shelf cavity mooring (Hattermann et al., 2012). Nivlisen is in comparison relatively thin (Fig. 2b) and we have no melt observations from the thicker ice in the southern areas. Grounding-line ice drafts (Fig. 1b), derived from Fretwell et al. (2013) and Mouginot et al. (2017), have an average value of 350 m. The deepest part of the grounding line (630 ± 100 m) is located at the outflow of Potsdam Glacier (Fig 1b), where higher basal melt rates may occur. In addition, Nivlisen has three ice-front sections, separated by ice rises and ice rumples, where the ocean can gain access to the inner parts of the ice-shelf cavity. At Fimbulisen, Hattermann et al. (2012, 2014) found that a

portion of the westward flowing coastal current was diverted under the ice shelf between two ice rises. Similar inflow pathways may also exist beneath the ice-front sections of Nivlisen, explaining the variations of basal melt rates along profile A (Fig. 2a). At Fimbulisen, higher basal melt rates (3 m $yr^{-1}$) were also observed and modelled close to the ice front at shallow depths (< 200 m; Hattermann et al., 2014; Langley et al., 2014b), which is consistent with our results.

In the low-frequency radar profiles, we observed several undulating ice-base features (profile A and B; Fig. 3), where the englacial layers warp downwards, which is likely an indication of basal channels or crevasses. The southernmost measurement in profile B is located at one of these down-warping features, where surface elevation is slightly lowered locally (–0.5 m). Higher basal melt rates were not observed here compared with the surrounding sites, although, higher melt rates typically occur on the flanks of basal channels, rather than at their apex (Berger et al., 2017). The channel may have formed at an upstream ice rumple and been passively advected downstream (Fig. 2a). Basal channels are important features influencing the ice-shelf stability, since they affect ice-shelf cavity circulation and play a role in the exchange of heat and mass between the ocean and ice shelf (Gladish et al., 2012; McGrath et al., 2012; Millgate et al., 2013; Stanton et al., 2013). Basal channels are not restricted to rapidly melting ice shelves and have been observed elsewhere in Dronning Maud Land, at Fimbulisen (Langley et al., 2014a) and Roi Baudouin Ice Shelf (Fig. 1a; Berger et al., 2017). Detailed studies of these features together with basal melting are needed to understand their initiation, evolution, and role in the overall mass balance of ice shelves (Alley et al., 2016).

## 5.2 Temporal variations in melting

Basal melt rates at Nivlisen varied on a broad range of timescales (Fig. 4 and 5). At the seaward site, we observed a seasonal signal, where the monthly averaged basal melt rates were two to three times higher in the summer than in winter (Fig. 4a, Supplements Fig. S3). At the landward site, we observed no seasonal pattern, however, some variability on monthly time scales was present (Fig. 5a, Supplements Fig. S3). We performed a continuous wavelet transform on the time-series data from the two overwintering sites, based on the method and software package provided by Grinsted et al. (2004). The wavelet transform is used to study localized

intermittent periodicities, in contrast to more traditional mathematical methods, such as Fourier analysis, which assumes that the underlying process is stationary in time. We used a Morlet wavelet with $\omega_0 = 6$, which provides a good balance between time and frequency localization. The wavelet transform shows the normalized thinning rates at different scales to identify dominant periods of variability in time (Fig. 4b, 5b). The statistical significance was assessed relative to the null hypothesis, modelled by a first order autoregressive process. The wavelet transform has edge artefacts since it is not completely localized in time, as indicated by the cone of influence, masking out low frequency signals at the beginning and end of the time series. The thinning variability at diurnal timescales, and to some extent semi-diurnal timescales, varied at an approximately two-weekly period. This reflects the fortnightly spring-neap tidal cycle at which the strength of the tidal currents varies because of the interference of different constituents, usually $M_2$ and $S_2$ in this area (plotted as white dashed lines in Fig. 4b and 5b). Stronger tidal currents increase the heat exchange at the ice-ocean interface and may hence cause more rapid melt. At periods shorter than 36 hours, however, we cannot differentiate the strain signal from the melt signal. We also see some evidence of a slower variability in the data centred on 2–4 days (Fig. 4d and 5d), which may be a result of mesoscale activity passing by the site (eddies or internal waves), which then show up in the melt rate. This is to some extent supported by Fourier analysis of the normalized 36 h filtered basal melt rates, which show peaks in power spectral density at 2–4 days, mostly visible at the seaward site (Supplements Fig. S4).

At the landward site, we observed no increased melting in summer, but we observed one melt peak in winter (12 June 2018; Fig. 5a). The melt event may have been caused by pulses of modified warm deep water reaching the base of the ice shelf as described by Hattermann et al. (2012), but it could also relate to other mesoscale activities within the cavity. In any case, the isolated event and the generally low basal melt rates suggest that warm deep water had limited access to the base of Nivlisen during 2017 and 2018. The observation is consistent with earlier studies, showing that ice-shelf cavities in this region are mainly filled with cold and fresh eastern shelf water (Nicholls et al., 2006; Thompson et al., 2018). Many factors control the extent to which warm deep water can access the ice-shelf cavities in Dronning Maud Land, such as the stability of the Antarctic slope front, local circulation, and bathymetry, and this has to be studied in more detail.

We studied the coherency between the two overwintering melt sites in a wavelet coherence (Grinsted et al., 2004) for the overlapping time periods in 2017 (Fig. 6). The wavelet coherence analysis finds significant coherence even if the common power is low, and it shows significant confidence levels against red noise backgrounds. Locally phase-locked behaviour can also be revealed; at weekly to monthly periods (7–30 days) in summer to fall (Jan–Apr 2017) the basal melt rates were in phase, whereas in winter (Apr–Jun) the melting at the seaward site led the increased signal, preceding the melt at the landward site. In late winter (Sept), the phase shifted to the landward site leading the melt. At Fimbulisen, the inflow of summer-warmed Antarctic surface water was observed at moorings close to the ice-shelf front with a clear seasonal signal in water temperatures and salinity (Hattermann et al., 2012). Hattermann et al. (2014) suggested that Antarctic surface water can reside for several months below the ice-shelf cavity, after initially being subducted beneath the ice front, potentially affecting basal melting deep inside the cavity. The observed melt rate pattern beneath Nivlisen may be an indication of similar movement of water masses below the ice shelf and further observations and modelling is needed to study these processes, currently being hampered by the lack of knowledge of bathymetry beneath the ice shelf.

We compared the basal melt rates with atmospheric ERA5 reanalysis data of wind speed, wind direction, air temperature, and sea-ice cover (Fig. 7) produced by the European Centre for Medium-Range Weather Forecasts (Copernicus Climate Change Service (C3S), 2017) at a grid point 10 km north of the ice-shelf front (Fig. 1b). ERA5 wind speeds at Nivlisen varied on daily timescales, ranging from 0 to 28 m $s^{-1}$. Winds generally blew from the east (Fig. 7b), corresponding to the pressure gradients imposed by the cyclonic system that dominates the Weddell Sea. As wind forcing can play an important role in downwelling and transportation of summer-warmed Antarctic surface water into the ice-shelf cavity (Zhou et al., 2014), we calculated the coherence between the normalized basal melt rates at the seaward site and wind speeds during time periods when there was open water in front of the ice shelf (grey area in Fig. 7a). The statistical significance level was estimated using Monte Carlo simulation with a Fourier transform method, where a large set of surrogate data-set pairs were generated using phase randomization (Schreiber and Schmitz, 2000). We found a significant coherence between basal melt rates and wind speeds ($r = 0.35$, $p < 0.01$; Fig. 8). We found no such coherence in winter.

462 The variability in winter may be due to the transport mainly dominated by eddies, shed by
463 instabilities in the along-slope current. We also compared individual melt peaks in summer with
464 higher wind events (dashed vertical lines in Fig. 7). The melt peaks have a time lag of ~0 to 3
465 days after a wind event. Air temperatures at 2 m varied mostly on seasonal time scales, with
466 temperatures between 0 and −10° C in summer, when we observe the highest basal melting, and
467 down to −28° C in winter (Fig. 7c). The temperature variability in the reanalysis data on shorter
468 timescales agreed with our weather station on Leningradkollen ice rise (190 m a.s.l.), however,
469 the seasonal temperature signal had a lower amplitude than at the weather station, which
470 measured temperatures down to −38° C. When air temperatures were high and basal melt rates
471 increased in early summer at the seaward site (Dec 2016 and 2017), we observed open water
472 close to Nivlisen, which is the time when solar radiation may warm the surface waters (Fig. 7).
473 Sea ice is widespread in front of the ice shelf during winter and then breaks up during summer
474 typically starting from the west and progressing to the more sheltered eastern side (Supplements
475 Fig. S5). The general pattern of summer retreat is interrupted by irregular periods of some sea ice
476 re-growth (e.g. early February 2017 and 2018; Fig. S5). Similar seasonally higher basal melt
477 rates (up to ~5 m $yr^{-1}$) were observed at Ross Ice Shelf in West Antarctica, where solar-heated
478 surface water in a polynya near the ice front was linked to the higher melt rates; however, they
479 did not find any link to downwelling-favourable winds, but rather density gradients caused by
480 seasonal brine release in the polynya (Stewart et al., 2019).

481 In summary, the basal melt rates varied on seasonal, monthly, and daily timescales
482 related to the tidal cycles and mesoscale activities in the ice-shelf cavity. We hypothesize that
483 summer-warmed Antarctic surface water was pushed by wind under the front of the ice shelf.
484 Reduced sea-ice cover and higher wind speeds may increase melting from surface waters, while
485 weaker winds and/or changes in the surface buoyancy forcing may increase exposure of the ice-
486 shelf cavities to warm deep water. Surface winds are projected to intensify over the next century
487 with increased greenhouse gas emissions (Greene et al., 2017) and extreme changes in sea-ice
488 extent have occurred in recent years (Shepherd et al., 2018). Warming of the surface water is
489 projected to increase ice-shelf melting along Dronning Maud Land in future climate scenarios
490 (Kusahara and Hasumi, 2013) and recent studies suggest that non-linear feedbacks may facilitate
491 an irreversible transition into a state of higher melting in the Weddell Sea (Hattermann, 2018;

Hellmer et al., 2017). Increases in basal melting will tend to thin the ice shelves and reduce the buttressing on the inland ice sheet. It remains to be understood to what extent, increased summer-warmth driven melting, intensified in the vicinity of pinning points may affect the ice flow dynamics and ice-shelf stability.

## 6 Conclusions

We present a two year record of basal melting at Nivlisen in Dronning Maud Land, East Antarctica, at high spatial and temporal resolution using in situ phase-sensitive radar measurements. Averaged annual basal melt rates are in general moderate (0.8 m $yr^{-1}$), but relatively high melt rates were observed close to a grounded feature near the ice-shelf front. Hourly measurements also reveal a seasonal melt pattern close to the ice-shelf front, where the highest basal melt rates occurred in summer (5.6 m $yr^{-1}$). Comparing the seasonality in basal melting with forcing from atmospheric reanalysis data, we found that the variability in the basal melt is likely caused by summer-warmed surface water pushed by wind into the ice-shelf cavity. Farther into the ice-shelf cavity, we observe a different melt regime, with significantly lower basal melt rates and a clearer tidal signal. We conclude that warm deep ocean water has a limited effect on the basal melting of Nivlisen, likely because the present configuration of the Antarctic slope front, which separates the deeper water from the continent, protects the ice shelf from those warmer water masses. Our study highlights that, although many of the ice shelves in East Antarctica have generally low basal melt rates, their seaward sections have temporally higher basal melt rates due to the influence of summer-warmed surface waters. The frontal areas are stabilized by pinning points and these areas could potentially be sensitive to future change if the basal rates would increase. We demonstrate the use of and need for continuous in situ monitoring of Antarctic ice shelves to resolve variability in basal melting that is not captured in satellite data. Long-term, high-resolution time-series data are crucial to understand the complex mechanisms involved in ice shelf–ocean interactions.

## Data availability

The compiled data sets of basal melt rates, strain rates, ice flow velocity, surface mass balance, and ice thickness from low-frequency radar profiling are available at the project webpage (https://www.npolar.no/prosjekter/madice/) and Norwegian Polar Data Centre portal (https://data.npolar.no).

## Author contribution

KL led the overall data analysis and interpretations and prepared the paper with contributions from all co-authors. KL, GM, and BP collected the ApRES, ice flow, and surface mass balance data. KWN was responsible for the ApRES system setup. KM was responsible for the low-frequency radar system and collected the data. TH contributed to the discussion section. MT and KM were the project leaders.

## Competing interests

KM is a member of the editorial board of the journal.

## Acknowledgments

This work was part of the MADICE (Mass balance, dynamics, and climate of the central Dronning Maud Land coast, East Antarctica) project, funded by the Research Council of Norway (project 248780) and the Ministry of Earth Sciences, India (project MoES/Indo-Nor/PS-3/2015). We would like to thank the NCPOR and NPI logistic heads and personnel who helped us in the field. We also thank Chris Borstad for estimating flowlines to the ice rumple, Harvey Goodwin for assessing field safety, Vikram Goel for helping collect the data in field, and Robert Graham for providing the ERA5 data. Figures 1 and 2 were prepared using Quantarctica (quantarctica.npolar.no). For the REMA data set we acknowledge the following: DEMs provided by the Byrd Polar and Climate Research Center and the Polar Geospatial Center under NSF-OPP awards 1543501, 1810976, 1542736, 1559691, 1043681, 1541332, 0753663, 1548562, 1238993

and NASA award NNX10AN61G. Computer time provided through a Blue Waters Innovation Initiative. DEMs produced using data from DigitalGlobe, Inc. We thank the two anonymous reviewers and the editor Nanna B. Karlsson for their valuable suggestions and comments.

## References

Adusumilli, S., Fricker, H. A., Siegfried, M. R., Padman, L., Paolo, F. S. and Ligtenberg, S. R. M.: Variable Basal Melt Rates of Antarctic Peninsula Ice Shelves, 1994-2016, Geophys. Res. Lett., 45, 4086–4095, doi:10.1002/2017GL076652, 2018.

Alley, K. E., Scambos, T. A., Siegfried, M. R. and Fricker, H. A.: Impacts of warm water on Antarctic ice shelf stability through basal channel formation, Nat. Geosci., 9, 290, 2016.

Anschütz, H., Eisen, O., Oerter, H., Steinhage, D. and Scheinert, M.: Investigating small-scale variations of the recent accumulation rate in coastal Dronning Maud Land , East Antarctica, Ann. Glaciol., 46, 14–21, 2007.

Arndt, J. E., Schenke, H. W., Jakobsson, M., Nitsche, F. O., Buys, G., Goleby, B., Rebesco, M., Bohoyo, F., Hong, J., Black, J., Greku, R., Udintsev, G. and Barrios, F.: The International Bathymetric Chart of the Southern Ocean (IBCSO) Version 1.0 — A new bathymetric compilation covering circum-Antarctic waters, Geophys. Res. Lett., 40, 3111–3117, doi:10.1002/grl.50413, 2013.

Bamber, J. L., Westaway, R. M., Marzeion, B. and Wouters, B.: The land ice contribution to sea level during the satellite era, Environ. Res. Lett., 13, 2018.

van de Berg, W. J., van den Broeke, M. R., Reijmer, C. H. and van Meijgaard, E.: Reassessment of the Antarctic surface mass balance using calibrated output of a regional atmospheric climate model, J. Geophys. Res., 111, 1–15, doi:10.1029/2005JD006495, 2006.

Berger, S., Drews, R., Helm, V., Sun, S. and Pattyn, F.: Detecting high spatial variability of ice-shelf basal mass balance, Roi Baudouin Ice Shelf, Antarctica, Cryosph., 11, 2675–2690, doi:10.5194/tc-2017-41, 2017.

Bindschadler, R., Vornberger, P., Fleming, A., Fox, A., Mullins, J., Binnie, D., Jean, S.,

Granneman, B. and Gorodetzky, D.: Remote Sensing of Environment The Landsat Image Mosaic of Antarctica, Remote Sens. Environ., 112(12), 4214–4226, doi:10.1016/j.rse.2008.07.006, 2008.

Borstad, C. P., Rignot, E., Mouginot, J. and Schodlok, M. P.: Creep deformation and buttressing capacity of damaged ice shelves : theory and application to Larsen C ice shelf, Cryosph., 7, 1931–1947, doi:10.5194/tc-7-1931-2013, 2013.

Brennan, P. V, Lok, L. B., Nicholls, K. and Corr, H.: Phase-sensitive FMCW radar system for high-precision Antarctic ice shelf profile monitoring, IET Radar Sonar Navig., 8(7), 776–786, doi:10.1049/iet-rsn.2013.0053, 2014.

British Antarctic Survey: Instrument: Phase-sensitive radar (ApRES), Filchner Ice Shelf, [online] Available from: https://www.bas.ac.uk/polar-operations/sites-and-facilities/facility/phase-sensitive-radar-apres/ (Accessed 13 November 2018), 2018.

Copernicus Climate Change Service (C3S): ERA5: Fifth generation of ECMWF atmospheric reanalyses of the global climate, Copernicus Clim. Chang. Serv. Clim. Data Store [online] Available from: https://www.ecmwf.int/en/forecasts/datasets/reanalysis-datasets/era5 (Accessed 1 November 2018), 2017.

Corr, H. F. J., Jenkins, A., Nicholls, K. W. and Doake, C. S. M.: Precise measurement of changes in ice-shelf thickness by phase-sensitive radar to determine basal melt rates, Geophys. Res. Lett., 29(8), 1–4, 2002.

Darelius, E. and Sallée, J. B.: Seasonal Outflow of Ice Shelf Water Across the Front of the Filchner Ice Shelf, Weddell Sea, Antarctica, Geophys. Res. Lett., 45, 3577–3585, doi:10.1002/2017GL076320, 2017.

Davis, P. E. D., Jenkins, A., Nicholls, K. W., Brennan, P. V, Povl, E., Heywood, K. J., Dutrieux, P., Cho, K. and Wan, T.: Variability in Basal Melting Beneath Pine Island Ice Shelf on Weekly to Monthly Timescales, J. Geophys. Res. Ocean., doi:10.1029/2018JC014464, 2018.

Depoorter, M. A., Bamber, J. L., Griggs, J. A., Lenaerts, J. T. M., Ligtenberg, S. R. M., Broeke, M. R. Van Den and Moholdt, G.: Calving fluxes and basal melt rates of Antarctic ice shelves, Nature, 502(7469), 89–92, doi:10.1038/nature12567, 2013.

Dong, J., Speer, K. and Jullion, L.: The Antarctic Slope Current near 30 deg E, J.

601 Geophys. Res. Ocean., 121, 1051–1062, 2016.

602 Dowdeswell, J. A. and Evans, S.: Investigations of the form and flow of ice sheets and
603 glaciers using radio-echo sounding, Reports Prog. Phys., 67(10), 1821–1861, doi:10.1088/0034-
604 4885/67/10/R03, 2004.

605 Dupont, T. K. and Alley, R. B.: Assessment of the importance of ice-shelf buttressing to
606 ice-sheet flow, Geophys. Res. Lett., 32, 1–4, doi:10.1029/2004GL022024, 2005.

607 Fretwell, P., Pritchard, H. D., Vaughan, D. G., Bamber, J. L., Barrand, N. E., Bell, R.,
608 Bianchi, C., Bingham, R. G., Blankenship, D. D., Casassa, G., Catania, G., Callens, D., Conway,
609 H., Cook, A. J., Corr, H. F. J., Damaske, D., Damm, V., Ferraccioli, F., Forsberg, R., Fujita, S.,
610 Gim, Y., Gogineni, P., Griggs, J. A., Hindmarsh, R. C. A., Holmlund, P., Holt, J. W., Jacobel, R.
611 W., Jenkins, A., Jokat, W., Jordan, T., King, E. C., Kohler, J., Krabill, W., Riger-Kusk, M.,
612 Langley, K. A., Leitchenkov, G., Leuschen, C., Luyendyk, B. P., Matsuoka, K., Mouginot, J.,
613 Nitsche, F. O., Nogi, Y., Nost, O. A., Popov, S. V, Rignot, E., Rippin, D. M., Rivera, A.,
614 Roberts, J., Ross, N., Siegert, M. J., Smith, A. M., Steinhage, D., Studinger, M., Sun, B., Tinto,
615 B. K., Welch, B. C., Wilson, D., Young, D. A., Xiangbin, C. and Zirizzotti, A.: Bedmap2:
616 improved ice bed, surface and thickness datasets for Antarctica, Cryosph., 7(1), 375–393,
617 doi:10.5194/tc-7-375-2013, 2013.

618 Gille, S. T.: Warming of the Southern Ocean Since the 1950s, Science, 295, 1275–1278,
619 2002.

620 Gingele, F. X., Kuhn, G., Maus, B., Melles, M. and Schöne, T.: Holocene ice retreat from
621 the Lazarev Sea shelf, East Antarctica, Cont. Shelf Res., 17(2), 137–163, 1997.

622 Gladish, C. V., Holland, D. M., Holland, P. R. and Price, S. F.: Ice-shelf basal channels in
623 a coupled ice/ocean model, J. Glaciol., 58(212), 1227–1244, doi:10.3189/2012JoG12J003, 2012.

624 Greene, C. A., Blankenship, D. D., Gwyther, D. E., Silvano, A. and Wijk, E. Van: Wind
625 causes Totten Ice Shelf melt and acceleration, Sci. Adv., 3, 1–5, doi:10.3934/mbe.2012.9.125,
626 2017.

627 Grinsted, A., Moore, J. C. and Jevrejeva, S.: Application of the cross wavelet transform
628 and wavelet coherence to geophysical time series, Nonlinear Process. Geophys., 11(5/6), 561–

566, doi:10.5194/npg-11-561-2004, 2004.

Hattermann, T.: Antarctic Thermocline Dynamics along a Narrow Shelf with Easterly Winds, J. Phys. Oceanogr., 48, 2419–2442, doi:10.1175/JPO-D-18-0064.1, 2018.

Hattermann, T., Nøst, O. A., Lilly, J. M. and Smedsrud, L. H.: Two years of oceanic observations below the Fimbul Ice Shelf, Antarctica, Geophys. Res. Lett., 39(L12605), doi:10.1029/2012GL051012, 2012.

Hattermann, T., Smedsrud, L. H., Nøst, O. A., Lilly, J. M. and Galton-fenzi, B. K.: Eddy-resolving simulations of the Fimbul Ice Shelf cavity circulation: Basal melting and exchange with open ocean, Ocean Model., 82, 28–44, doi:10.1016/j.ocemod.2014.07.004, 2014.

Hazel, J. E. and Stewart, A. L.: Are the Near-Antarctic Easterly Winds Weakening in Response to Enhancement of the Southern Annular Mode?, J. Clim., 32(6), 1895–1918, doi:10.1175/jcli-d-18-0402.1, 2019.

Hellmer, H. ., Kauker, F., Timmermann, R. and Hattermann, T.: The Fate of the Southern Weddell Sea Continental Shelf in a Warming Climate, J. Clim., 30, 4337–4350, doi:10.1175/JCLI-D-16-0420.1, 2017.

Heywood, K. J., Locarnini, R. A., Frew, R. D., Dennis, P. F. and King, B. A.: Transport and water masses of the Antarctic slope front system in the eastern Weddell Sea, Ocean. Ice, Atmos. Interact. Antarct. Cont. Margin, 24(January), 203–214, doi:10.1029/ar075p0203, 1998.

Hogg, A. E. and Gudmundsson, G. H.: Impacts of the Larsen-C Ice Shelf calving event, Nat. Clim. Chang., 7, 540–542, doi:10.1038/nclimate3359, 2017.

Horwath, M., Dietrich, R., Baessler, M., Nixdorf, U., Steinhage, D., Fritzsche, D., Damm, V. and Reitmayr, G.: Nivlisen, an Antarctic ice shelf in Dronning Maud Land: geodetic – glaciological results from a combined analysis of ice thickness, ice surface height and ice-flow observations, J. Glaciol., 52(176), 17–30, 2006.

Howat, I. M., Porter, C., Smith, B. E., Noh, M. J. and Morin, P.: The Reference Elevation Model of Antarctica, Cryosph., 13, 665–674, doi:10.5194/tc-13-665-2019, 2019.

Irving, J. D., Knoll, M. D. and Knight, R. J.: Improving crosshole radar velocity

656 tomograms: A new approach to incorporating high-angle traveltime data, Geophysics, 72(4), 31–
657 41, doi:10.1190/1.2742813, 2007.

658 Jacobs, S. S., Helmer, H. H., Doake, C. S. M., A, J. and Frolich, R. M.: Melting of ice
659 shelves and the mass balance of Antarctica, J. Glaciol., 38(130), 375–387, 1992.

660 Jenkins, A. and Doake, C. S. M.: Ice-ocean interaction on Ronne Ice Shelf, Antarctica, J.
661 Geophys. Res. Ocean., 96(C1), 791–813, doi:10.1029/90JC01952, 1991.

662 Jenkins, A., Corr, H. F. J., Nicholls, K. W., Stewart, C. L. and Doake, C. S. M.:
663 Interactions between ice and ocean observed with phase-sensitive radar near an Antarctic ice-
664 shelf grounding line, J. Glaciol., 52(178), 325–346, 2006.

665 Joughin, I. and Vaughan, D. G.: Marine ice beneath the Filchner-Ronne Ice Shelf,
666 Antarctica: a comparison of estimated thickness distributions, Ann. Glaciol., 39, 511–517, 2004.

667 Kingslake, J., Ng, F. and Sole, A.: Modelling channelized surface drainage of
668 supraglacial lakes, J. Glaciol., 61(225), 185–199, doi:10.3189/2015JoG14J158, 2015.

669 Kusahara, K. and Hasumi, H.: Modeling Antarctic ice shelf responses to future climate
670 changes and impacts on the ocean Ž , J. Geophys. Res. Ocean., 118, 2454–2475,
671 doi:10.1002/jgrc.20166, 2013.

672 Kwok, R. and Comiso, J.: Southern Ocean Climate and Sea Ice Anomalies Associated
673 with the Southern Oscillation, J. Clim., 15, 487–501, 2002.

674 Kwok, R., Comiso, J. C., Lee, T. and Holland, P. R.: Linked trends in the South Pacific
675 sea ice edge and Southern Oscillation Index, J. Geophys. Res., 43, 295–302,
676 doi:10.1002/2016GL070655.Received, 2016.

677 Langley, K., von Deschwanden, A., Kohler, J., Sinisalo, A., Matsuoka, K., Hattermann,
678 T., Humbert, A., Nøst, O. A. and Isaksson, E.: Complex network of channels beneath an
679 Antarctic ice shelf, Geophys. Res. Lett., 41, 1209–1215, 2014a.

680 Langley, K., Kohler, J., Sinisalo, A., Øyan, M. J., Hamran, S. E., Hattermann, T.,
681 Matsuoka, K., Nøst, O. A. and Isaksson, E.: Low melt rates with seasonal variability at the base
682 of Fimbul Ice Shelf, East Antarctica, revealed by in situ interferometric radar measurements,

683 Geophys. Res. Lett., 41(22), 8138–8146, doi:10.1002/2014GL061782, 2014b.

684 Lapazaran, J. J., Otero, J. and Navarro, F. J.: On the errors involved in ice-thickness
685 estimates I: ground- penetrating radar measurement errors, J. Glaciol., 1–13,
686 doi:10.1017/jog.2016.93, 2016.

687 Lenaerts, J. T. M., Brown, J., Broeke, M. R. V. A. N. D. E. N., Matsuoka, K., Drews, R.,
688 Callens, D., Philippe, M., Gorodetskaya, I. V, Meijgaard, E. V. A. N., Reijmer, C. H., Pattyn, F.
689 and Lipzig, N. P. M. V. A. N.: High variability of climate and surface mass balance induced by
690 Antarctic ice rises, J. Glaciol., 60(224), 1101–1110, doi:10.3189/2014JoG14J040, 2014.

691 Lenaerts, J. T. M., Lhermitte, S., Drews, R., Ligtenberg, S. R. M., Berger, S. and Helm,
692 V.: Meltwater produced by wind – albedo interaction stored in an East Antarctic ice shelf, Nat.
693 Clim. Chang., 7, 58–63, doi:10.1038/NCLIMATE3180, 2017.

694 Lindbäck, K., Pettersson, R., Doyle, S. H., Helanow, C., Jansson, P., Kristensen, S. S.,
695 Stenseng, L., Forsberg, R. and Hubbard, A. L.: High-resolution ice thickness and bed topography
696 of a land-terminating section of the Greenland Ice Sheet, Earth Syst. Sci. Data, 6, 331–338,
697 doi:doi:10.5194/essd-6-331-2014, 2014.

698 Lindbäck, K., Kohler, J., Pettersson, R., Nuth, C. and Langley, K.: Subglacial
699 topography, ice thickness, and bathymetry of Kongsfjorden, northwestern Svalbard, Earth Syst.
700 Sci. Data, 10, 1769–1781, 2018.

701 Makinson, K. and Nicholls, K. W.: Modeling tidal currents beneath Filchner-Ronne Ice
702 Shelf and on the adjacent continental shelf: Their effect on mixing and transport, J. Geophys.
703 Res. Ocean., 104(C6), 13449–13465, doi:10.1029/1999jc900008, 1999.

704 Malyarenko, A., Robinson, N. J., Williams, M. J. M. and Langhorne, P. J.: A wedge
705 mechanism for summer surface water inflow into the Ross Ice Shelf cavity, J. Geophys. Res.
706 Ocean., 1196–1214, doi:10.1029/2018jc014594, 2019.

707 Marsh, O. J., Fricker, H. A., Siegfried, M. R., Christianson, K., Nicholla, K. W., Corr, H.
708 F. J. and Catania, G.: High basal melting forming a channel at the grounding line of Ross Ice
709 Shelf, Antarctica, Geophys. Res. Lett., 43, 1–6, doi:10.1002/2015GL066612.Received, 2016.

710 Matsuoka, K., Pattyn, F., Callens, D. and Conway, H.: Radar characterization of the basal

711 interface across the grounding zone of an ice-rise promontory in East Antarctica, Ann. Glaciol.,
712 53(60), 29–34, doi:10.3189/2012AoG60A106, 2012.

713 McGrath, D., Steffen, K., Scambos, T., Rajaram, H., Casassa, G. and Rodriguez Lagos, J.
714 L.: Basal crevasses and associated surface crevassing on the Larsen C ice shelf, Antarctica, and
715 their role in ice-shelf instability, Ann. Glaciol., 53(60), 10–18, doi:10.3189/2012AoG60A005,
716 2012.

717 Millgate, T., Holland, P. R., Jenkins, A. and Johnson, H. L.: The effect of basal channels
718 on oceanic ice-shelf melting, J. Geophys. Res. Ocean., 118(September), 6951–6964,
719 doi:10.1002/2013JC009402, 2013.

720 Moholdt, G. and Matsuoka, K.: Inventory of Antarctic ice rises and rumples (version 1), ,
721 doi:10.21334/npolar.2015.9174e644, 2015.

722 Mouginot, J., Scheuchl, B. and Rignot., E.: MEaSUREs Antarctic Boundaries for IPY
723 2007-2009 from Satellite Radar, Version 2., NASA Natl. Snow Ice Data Cent. Distrib. Act.
724 Arch. Center., doi:https://doi.org/10.5067/AXE4121732AD, 2017.

725 Natural Resources Canada: CSRS-PPP: On-Line GNSS PPP Post-Processing Service,
726 [online] Available from: http://webapp.geod.nrcan.gc.ca/geod/tools-outils/ppp.php, 2017.

727 Nicholls, K. W., Abrahamsen, E. P., Buck, J. J. H., Dodd, P. A., Goldblatt, C., Griffiths,
728 G., Heywood, K. J., Hughes, N. E., Kaletzky, A., Mcphail, S. D., Millard, N. W., Oliver, K. I. C.,
729 Perrett, J., Price, M. R., Pudsey, C. J., Saw, K., Stansfield, K., Stott, M. J., Wadhams, P., Webb,
730 A. T. and Wilkinson, J. P.: Measurements beneath an Antarctic ice shelf using an autonomous
731 underwater vehicle, Geophys. Res. Lett., 33, doi:10.1029/2006GL025998, 2006.

732 Nicholls, K. W., Corr, H. F. J., Stewart, C. L., Lok, L. B., Brennan, P. V and Vaughan, D.
733 G.: Instruments and Methods A ground-based radar for measuring vertical strain rates and time-
734 varying basal melt rates in ice sheets and shelves, J. Glaciol., 61(230), 1079–1087,
735 doi:10.3189/2015JoG15J073, 2015.

736 Nøst, O. A., Biuw, M., Tverberg, V., Lydersen, C., Hattermann, T., Zhou, Q., Smedsrud,
737 L. H. and Kovacs, K. M.: Eddy overturning of the Antarctic Slope Front controls glacial melting
738 in the Eastern Weddell Sea, J. Geophys. Res. Ocean., 116(11), 1–17,

739 doi:10.1029/2011JC006965, 2011.

740 Paolo, F. S., Fricker, H. A. and Padman, L.: Volume loss from Antarctic ice shelves is
741 accelerating, Science, 348(6232), 327–332, 2015.

742 Pritchard, H. D., Ligtenberg, S. R. M., Fricker, H. A., Vaughan, D. G., Broeke, M. R.
743 Van Den and Padman, L.: Antarctic ice-sheet loss driven by basal melting of ice shelves, Nature,
744 484(7395), 502–505, doi:10.1038/nature10968, 2012.

745 Rahman, S.: FMCW Radar Signal Processing for Antarctic Ice Shelf Profiling and
746 Imaging, Unversity College London., 2016.

747 Reese, R., Gudmundsson, G. H., Levermann, A. and Winkelmann, R.: The far reach of
748 ice-shelf thinning in Antarctica, Nat. Clim. Chang., 8, 53–57, doi:10.1038/s41558-017-0020-x,
749 2018.

750 Rignot, E., Mouginot, J. and Scheucht, B.: Ice Flow of the Antarctic Ice Sheet, Science,
751 333(September), 1427–1431, 2011.

752 Rignot, E., Jacobs, S., Mouginot, J. and Scheuchl, B.: Ice-Shelf Melting Around
753 Antarctica, Science, 341, 266–270, 2013.

754 Rignot, E., Mouginot, J., Scheuchl, B., van den Broeke, M. R., van Wessem, M. J. and
755 Morlighem, M.: Four decades of Antarctic Ice Sheet mass balance from 1979-2017, Proc. Natl.
756 Acad. Sci., 1–9, doi:10.1073/pnas.1812883116, 2019.

757 Rintoul, S. R., Silvano, A., Pena-molino, B., Wijk, E. Van, Rosenberg, M., Greenbaum,
758 J. S. and Blankenship, D. D.: Ocean heat drives rapid basal melt of the Totten Ice Shelf, Sci.
759 Adv., 2, 1–5, 2016.

760 Ryan, S., Schröder, M., Huhn, O. and Timmermann, R.: On the warm inflow at the
761 eastern boundary of the Weddell Gyre, Deep. Res. Part I Oceanogr. Res. Pap., 107, 70–81,
762 doi:10.1016/j.dsr.2015.11.002, 2016.

763 De Santis, A., Maier, E., Gomez, R. and Gonzalez, I.: Antarctica, 1979–2016 sea ice
764 extent: total versus regional trends, anomalies, and correlation with climatological variables, Int.
765 J. Remote Sens., 38(24), 7566–7584, doi:10.1080/01431161.2017.1363440, 2017.

Schmidtko, S., Heywood, K. J., Thompson, A. F. and Aoki, S.: Multidecadal warming of Antarctic waters: Supplementary Material, Science, 346(6214), 1227–1231, doi:10.1126/science.1256117, 2014.

Schreiber, T. and Schmitz, A.: Surrogate time series, Phys. D, 142, 346–382, 2000.

Shepherd, A., Fricker, H. A. and Farrell, S. L.: Trends and connections across the Antarctic cryosphere, Nature, 558, 223–232, 2018.

Stanton, T. P., Shaw, W. J., Truffer, M., Corr, H. F. J., Peters, L. E., Riverman, K. L., Bindschadler, R. A., Holland, D. M. and Anandakrishnan, S.: Channelized Ice Melting in the, Science, 341(September), 1236–9, doi:10.1126/science.1239373, 2013.

Stern, A. A., Dinniman, M. S., Zagorodnov, V., Tyler, S. W. and Holland, D. M.: Intrusion of warm surface water beneath the McMurdo ice shelf, Antarctica, J. Geophys. Res. Ocean., 118(12), 7036–7048, doi:10.1002/2013JC008842, 2013.

Stewart, A. L. and Thompson, A. F.: Eddy Generation and Jet Formation via Dense Water Outflows across the Antarctic Continental Slope, J. Phys. Oceanogr., 46(12), 3729–3750, doi:10.1175/jpo-d-16-0145.1, 2016.

Stewart, C. L., Christoffersen, P., Nicholls, K. W., Williams, M. J. M. and Dowdeswell, J. A.: Basal melting of Ross Ice Shelf from solar heat absorption in an ice-front polynya, Nat. Geosci., 1(January), doi:10.1038/s41561-019-0356-0, 2019.

Stuecker, M., Bitz, C. and Armour, K.: Conditions leading to the unprecedented low Antarctic sea ice extent during the 2016 austral spring season, Geophys. Res. Lett., 44, 9008–9019, doi:10.1002/2017GL074691.Received, 2017.

Sverdrup, H. U.: The Currents off the Coast of Queen Maud Land, Nor. Geogr. Tidsskr. - Nor. J. Geogr., 14(1–4), 239–249, doi:10.1080/00291955308542731, 1954.

Swart, N. C., Gille, S. T., Fyfe, J. C. and Gillett, N. P.: Recent Southern Ocean warming and freshening driven by greenhouse gas emissions and ozone depletion, Nat. Geosci., 11, 836–842, doi:10.1038/s41561-018-0226-1, 2018.

Taylor, J. R.: An Introduction to Error Analysis: The Study of Uncertainties in Physical

Measurements, University of Colorado., 1996.

The IMBIE Team: Mass balance of the Antarctic Ice Sheet from 1992 to 2017, Nature, 558, 219–222, doi:10.1017/cbo9780511535659.014, 2018.

Thompson, A. F., Heywood, K. J., Schmidtko, S. and Stewart, A. L.: Eddy transport as a key component of the Antarctic overturning circulation, Nat. Geosci., 7(12), 879–884, doi:10.1038/ngeo2289, 2014.

Thompson, A. F., Stewart, A. L., Spence, P. and Heywood, K. J.: The Antarctic Slope Current in a Changing Climate, Rev. Geophys., 56(4), 741–770, doi:10.1029/2018RG000624, 2018.

Turner, J., Hosking, J. S., Bracegirdle, T. J., Marshall, G. J. and Phillips, T.: Recent changes in Antarctic Subject Areas, Philos. Trans. R. Soc. London, A 373(20140163), 2015.

Vaňková, I., Voytenko, D., Nicholls, K. W., Xie, S., Parizek, B. R. and Holland, D. M.: Vertical Structure of Diurnal Englacial Hydrology Cycle at Helheim Glacier, East Greenland, Geophys. Res. Lett., 45(16), 8352–8362, doi:10.1029/2018GL077869, 2018.

Zhou, Q., Hattermann, T., Nøst, O. A., Biuw, M., Kovacs, K. M. and Lydersen, C.: Wind-driven spreading of fresh surface water beneath ice shelves in the Eastern Weddell Sea, J. Geophys. Res. Ocean., 3818–3833, 2014.

## Figures

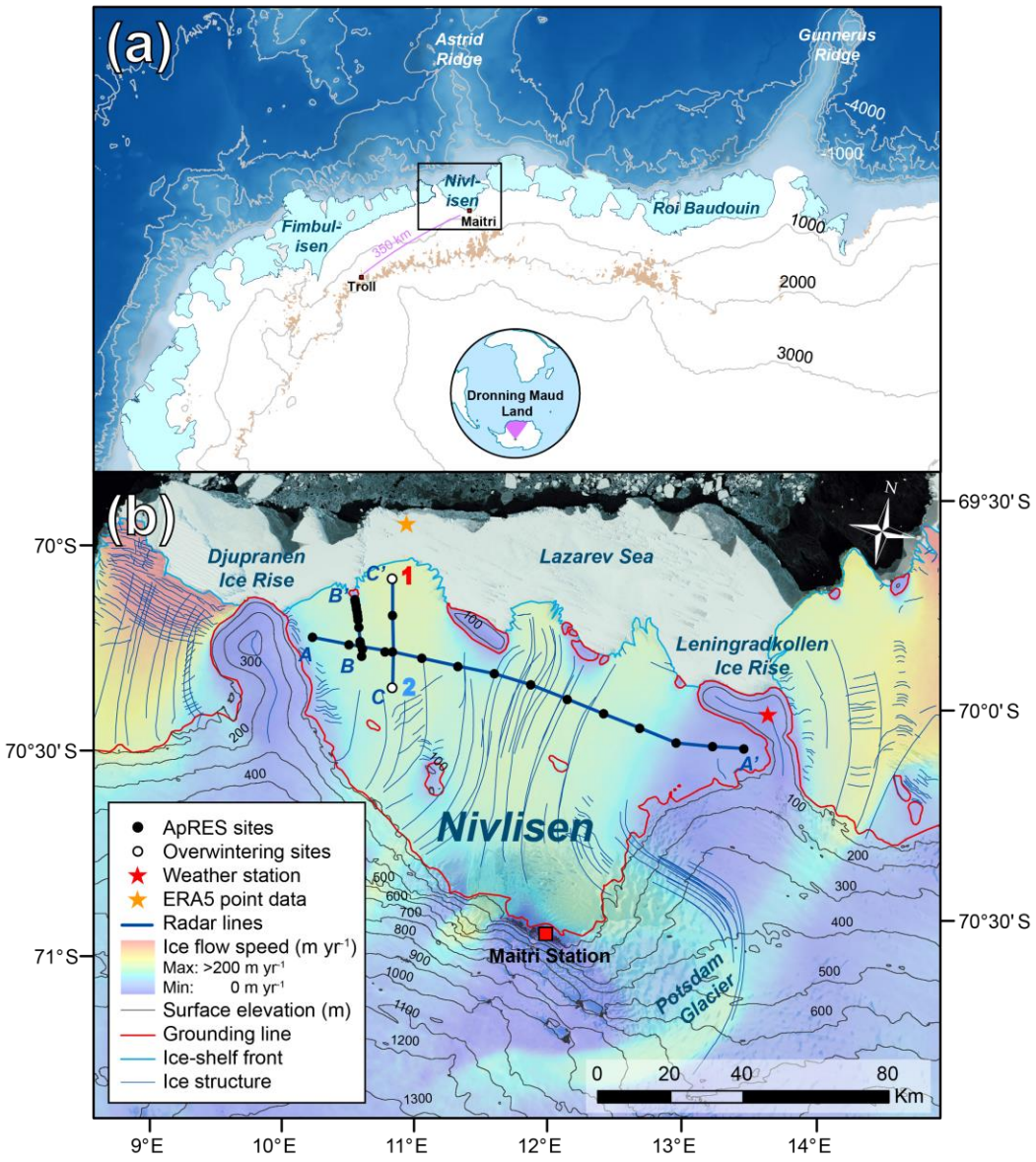


**Figure 1**. Study area: **(a)** Dronning Maud Land coast, with research stations (Troll and Maitri), ice shelves (light blue), and elevation contours with bathymetric features (Arndt et al., 2013). **(b)** Nivlisen ice shelf with surrounding areas. Study sites, where ApRES and stakes for ice velocity and surface mass balance were located, ApRES overwintering sites (no. 1 called "seaward" and no. 2 called "landward"), and low-frequency radar profiles (A, B, and C). Satellite derived ice speed (Rignot et al., 2011), surface elevation (m a.s.l.; Howat et al., 2019), grounding line, ice-shelf front (Mouginot et al., 2017), and ice structure (Goel et al., in review) are also shown. Background image is Landsat image mosaic with sea ice in front of the ice shelf (Bindschadler et al., 2008). Grid coordinate system is WGS-84.

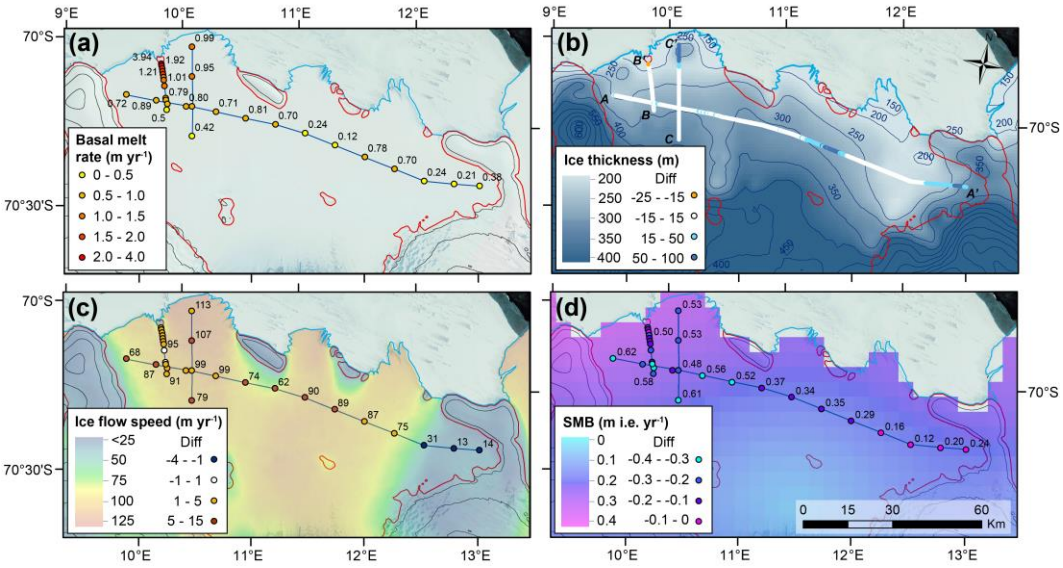


821

822 **Figure 2.** Comparison between in situ measured and satellite derived or modelled values: **(a)** ApRES-derived
823 averaged annual basal melt rates. See Supplements Fig. S2 for averaged annual basal melt rates for 2018, which is
824 on average within ±10 % from the 2017 values. **(b)** Ice thickness from Bedmap2 product (grid and contour lines;
825 Fretwell et al., 2013) and difference to low-frequency radar profiles (satellite derived minus measured in point
826 colour). **(c)** Ice flow speed from stakes (point numbers) and gridded satellite values (Rignot et al., 2011). Difference
827 (satellite derived minus measured) are shown in point colour. **(d)** Surface mass balance (SMB) from stakes (point
828 numbers) and gridded modelled values (van de Berg et al., 2006). Difference (modelled minus measured) are shown
829 in point colour. Background image and contour lines are the same as in Fig. 1.

830

831

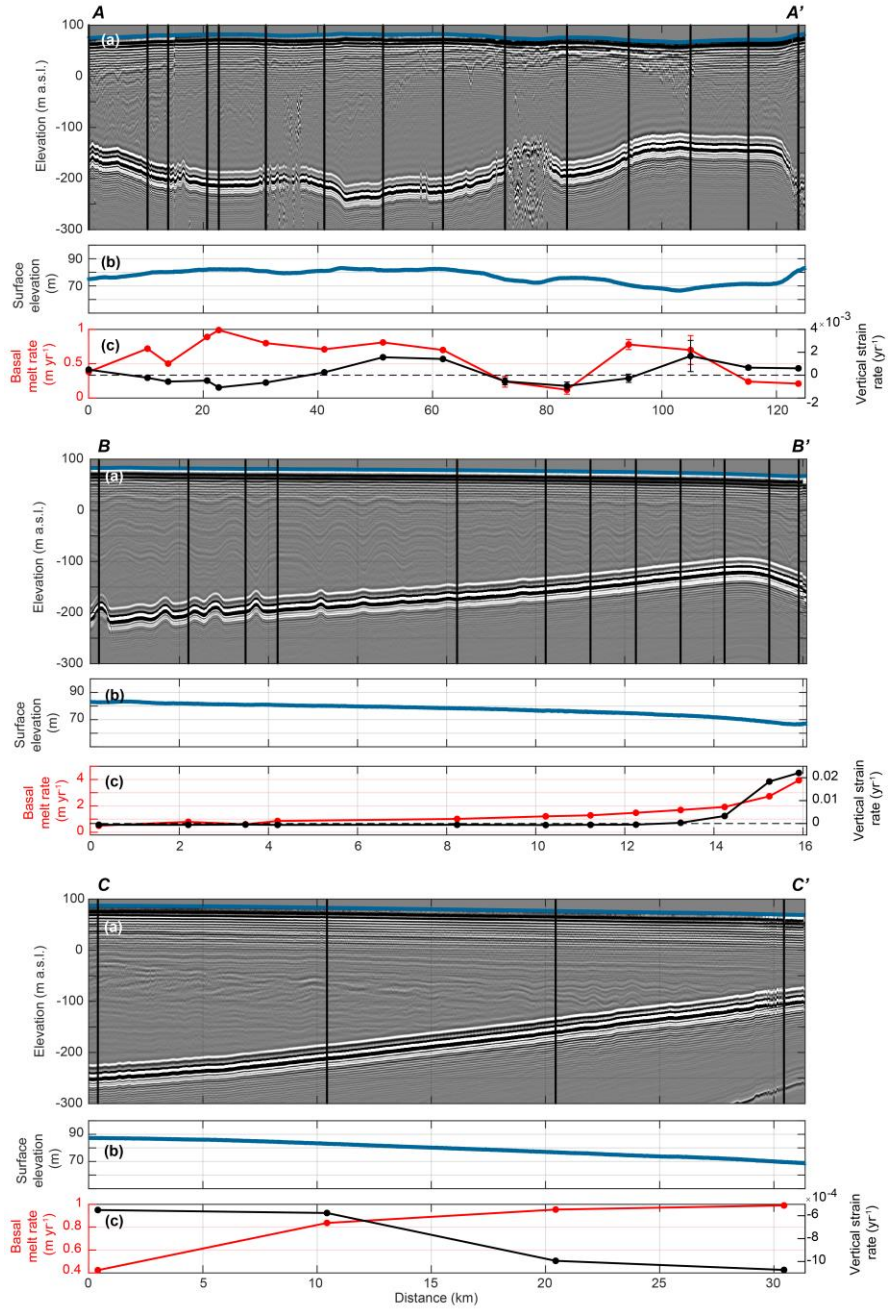


832

833 **Figure 3**. Profiles of low-frequency radar, ice surface elevation, basal melt, and strain (locations in Fig. 1b): A–A'
834 across ice flow from west to east (125 km), B–B' along ice flow from south to north towards an ice rumple (16 km),
835 and C–C' along ice flow from south to north out towards the ice front (32 km). Sub-panels show **(a)** radar profiles
836 with surface elevation (blue line), englacial stratigraphy, and basal elevation (grey tone shading), and locations of
837 ApRES measurements (black vertical lines), **(b)** surface elevation from carrier-phase kinematic GPS measurements,
838 and **(c)** annual basal melt rate (red) and vertical strain rates (black, dashed = 0) for 2017. Note that the x-axis scales
839 vary between the three profiles.

840

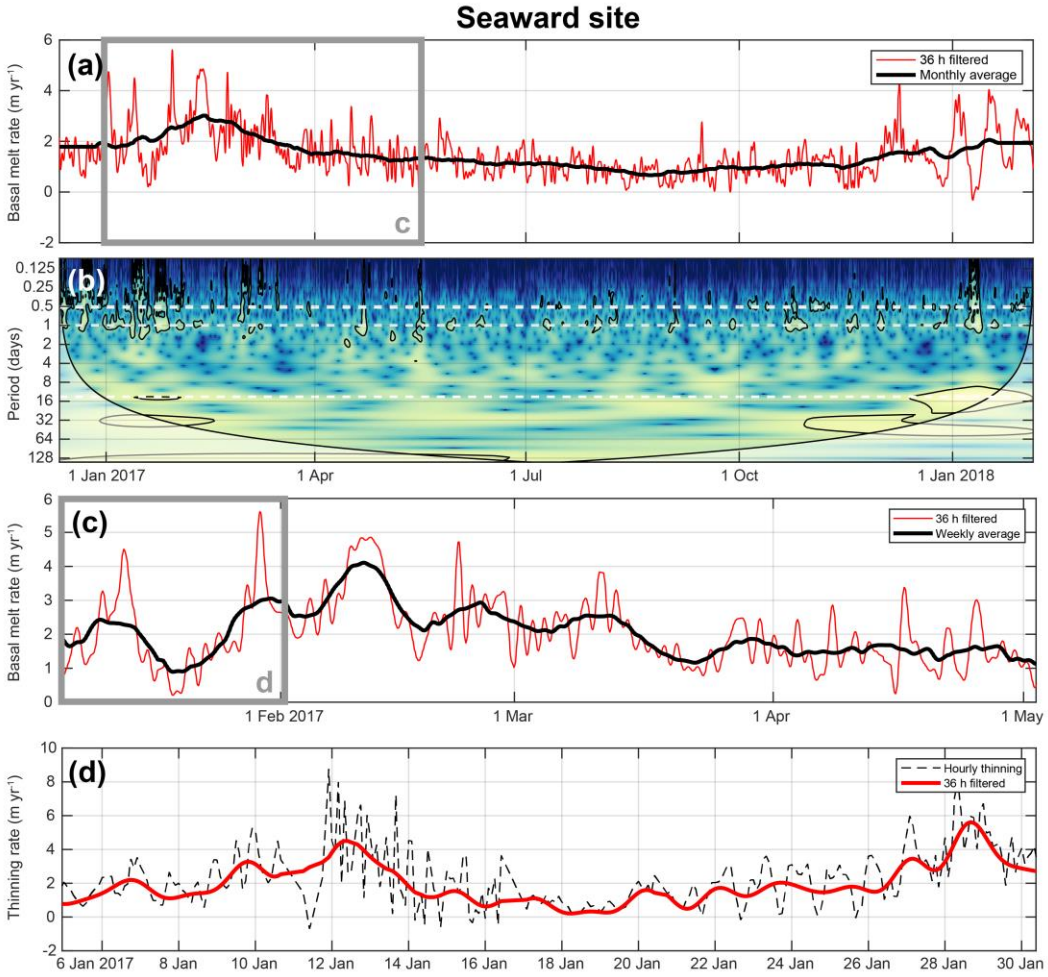


**Figure 4.** Basal melt and thinning rates for the seaward overwintering site, with variations on time scales of **(a)** months (11 Dec 2016–4 Feb 2018), **(c)** weeks (4 Jan–1 May 2017), and **(d)** days (1–31 Jan 2017). Dashed black line in (d) is the unfiltered raw data with thickness change including strain rates. **(b)** Continuous wavelet transform of the normalized thinning to identify the dominant modes of variability at different time scales. The left axis is the Fourier period. The colour shading represents the thinning associated with fluctuations over the course of the year with a particular time period (yellow = high power, blue = low power). The black contours delimit significant modes of variance at 95 % against red noise. Within the cone of influence, shown as a lighter shade in the right and left lower corners, edge effects may distort the image. Dashed white lines show the periods of major tidal constituents (0.5 d ≈ $K_1$, 1 d ≈ $M_2/S_2$, and 14 d ≈ $M_f$).

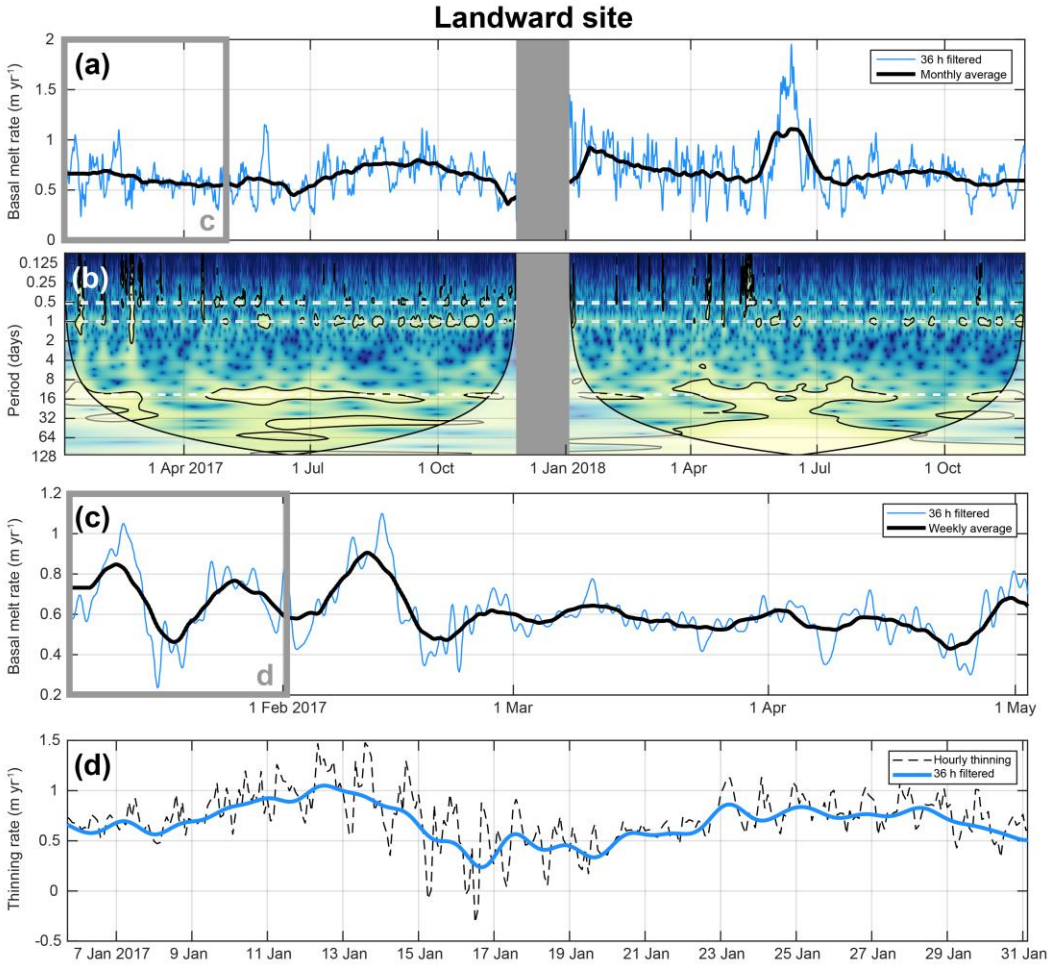


**Figure 5.** Basal melt and thinning rates for the landward overwintering site, with variations on time scales of **(a)** months (4 Jan 2017–27 Nov 2018), **(c)** weeks (4 Jan–1 May 2017), and **(d)** days (4–31 Jan 2017). **(b)** Continuous wavelet transform of the normalized thinning to identify the dominant modes of variability at different time scales. Grey box masks a time period with no data. See Fig. 4 caption for more information.

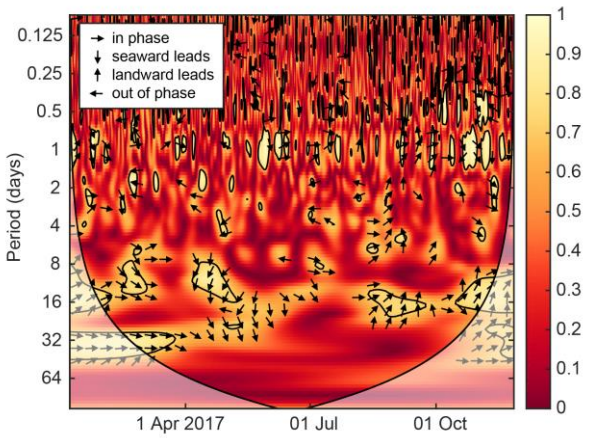


858

859 **Figure 6.** Wavelet coherence between overlapping time periods of the seaward and landward site (4 Jan–27 Nov
860 2017), showing times where the basal melt rates have common power. The phase relationship is shown as arrows. At
861 longer periods (8–30 days) in summer to fall (Jan–Apr) the signals are in phase, whereas in winter (Apr–Jun) the
862 melt at the seaward site leads the signal. In late winter (Sept) the phase shifts to the landward site leading the signal.
863 Within the cone of influence, shown as a lighter shade, edge effects become important.

864

865

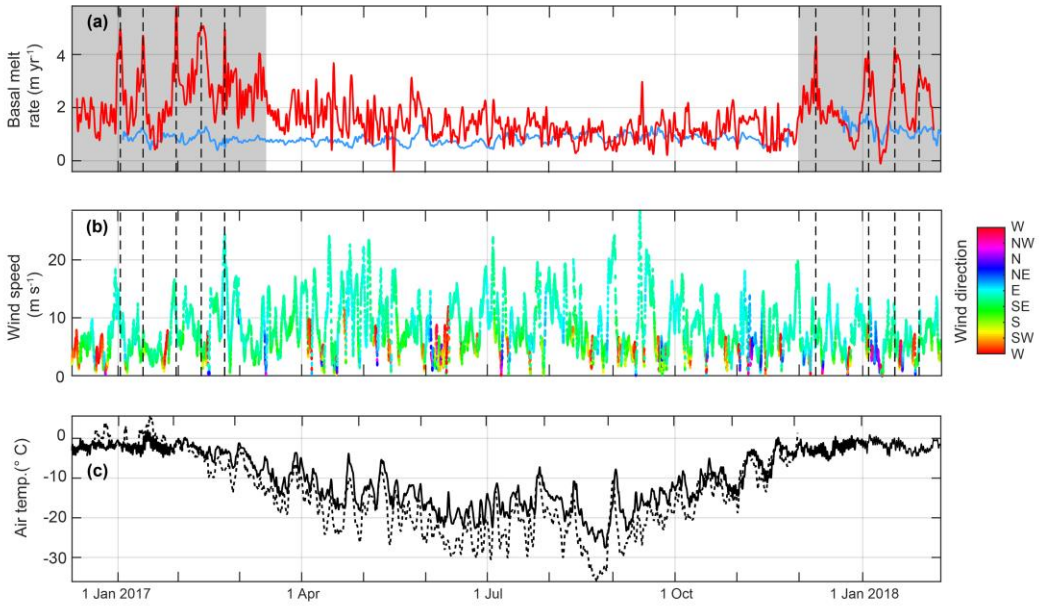


**Figure 7.** Basal melt rates compared with atmospheric forcing and sea-ice cover: **(a)** Thirty-six hour low-pass filtered basal melt rates at seaward site (red) and landward site (blue). Shaded grey area represents the time period in satellite data when there is open water in front of the ice shelf (Supplements Fig. S6). ERA5 reanalysis surface data of **(b)** wind speed and direction and **(c)** 2 m air temperature, where dashed black line is data from a nearby weather station (Fig. 1b). Vertical dashed lines show where time lags were calculated between basal melt and wind peaks.

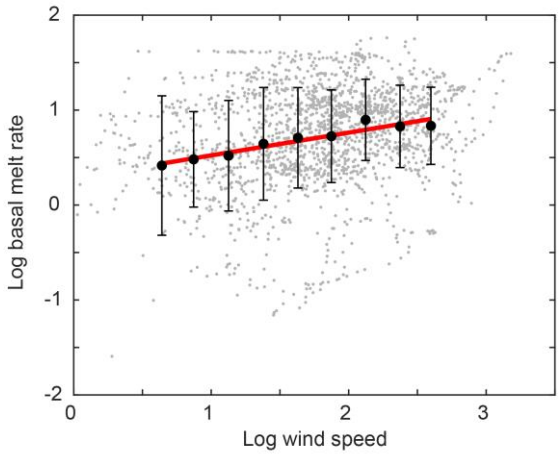


873

874 **Figure 8.** Scatter plot with the normalized basal melt rates at the seaward site and wind speeds for the time period
875 when there was open water in front of the ice shelf (grey area in Fig. 7a). Black points show average basal melt rate
876 calculated for each wind speed bin of 0.25 intervals. The red line shows the linear regression.

877